

Quasi-one-dimensional spin transport in antiferromagnetic Z^3 nodal net metals

Tingli He,^{1,2,*} Lei Li,^{2,*} Chaoxi Cui,² Run-Wu Zhang,² Zhi-Ming Yu,² Guodong Liu,¹ and Xiaoming Zhang¹

¹*School of Materials Science and Engineering, Hebei University of Technology, Tianjin 300130, China*

²*Key Lab of advanced optoelectronic quantum architecture and measurement (MOE), Beijing Key Lab of Nanophotonics & Ultrafine Optoelectronic Systems, and School of Physics, Beijing Institute of Technology, Beijing 100081, China*

In three dimensions, the quasi-one-dimensional (Q1D) transport is commonly thought to only appear in the systems with Q1D chain structure. Here, based on first-principle calculations, we go beyond the common belief to show that the Q1D transport can also be realized in many 3D antiferromagnetic (AFM) metals with topological node structure but without Q1D chain structure, including the existing compounds β -Fe₂(PO₄)O and Co₂(PO₄)O, and LiTi₂O₄. All these materials have an AFM ground state and exhibit an ideal crossed Z^3 Weyl nodal line in each spin channel, formed by three straight and flat nodal lines traversing the whole Brillouin zone. These nodal lines eventually lead to an AFM Z^3 nodal net. Surprisingly, we find that the longitudinal conductivity σ_{xx} in these topological nodal net metals is dozens of times larger than σ_{yy} and σ_{zz} in the up-spin channel, while σ_{yy} dominates the transport in the down-spin channel. This means that each spin channel has a Q1D transport signature, and the principal moving direction for the two spin channels is orthogonal, leading to Q1D direction-dependent spin transport. This novel phenomenon can not be found in both conventional 3D bulk materials and Q1D chain materials, and may solely be induced by the Z^3 nodal net, as it gradually disappears when the Fermi level moves away from the nodal net. Our work not only enhances the comprehension of topological physics in antiferromagnets, but also opens a new direction for the exploration of topological spintronics.

The coupling of magnetism and topological states have sparked widespread research interest [1–4]. Magnetic topological materials exhibit various novel physical properties, including quantum anomalous Hall effect [5–7], anomalous Hall effect [8–11], anomalous Nernst effect [11–15], and magnetoresistance effect [16, 17], which have potential application prospects in the field of spintronics. On one hand, magnetic ordering reduces the symmetry of the system as it breaks the time-reversal symmetry (\mathcal{T}) and certain crystal symmetries, making the extension of the topological phases to magnetic systems a challenging task [18–21]. On the other hand, magnetic ordering introduces an additional spin degree of freedom in the systems, providing new possibilities for achieving electric control of spin, a crucial task in the field of spintronics [22–24].

Various types of topological phases have been achieved in ferromagnetic (FM) systems, including kagome-lattice Co₃Sn₂S₂ [25], Heusler Co₂MnGa [26], rutile-type metal fluorides LiV₂F₆ [27], etc. These compounds exhibit special physical properties in the magnetic space group, including Weyl point and nodal line, as well as some anomalous magnetic transport properties, such as the massive Hall effect and anomalous thermal Hall effect. Recently, topological antiferromagnetic (AFM) spintronics, facilitated by AFM topological states, have garnered substantial interest [28, 29]. Contrasted with their FM counterparts, the absence of a macro-magnetic moment in AFM systems offers unique advantages for spintronics, such as the elimination of stray magnetic fields, de-

creased power requirements, and an elevated operating frequency response [30–32]. So far, different topological phases have been achieved in both collinear antiferromagnets and noncollinear antiferromagnets [33–43].

Recently, a novel kind of topological nodal line- Z^3 nodal line has been proposed in nonmagnetic systems [44]. The Z^3 nodal line traverses the whole Brillouin zone (BZ) and is characterized by three integers $Z^3 = (n_x, n_y, n_z)$, each indicating the number of times the line winds around the corresponding direction [44, 45]. Interestingly, due to the strong anisotropy, the ideal Z^3 nodal line is another structure besides layered and chain structures that can lead to low-dimensional transport phenomena. Here, the “ideal” means the Z^3 nodal line is straight and has a small energy variation, as illustrated in Fig. 1(a). For example, an ideal Z^3 nodal line with $n_z = 1$ would lead to a Q2D transport, as the velocity of the nodal-line electrons along the z -direction is much smaller than that on the x - y plane [see Fig. 1(a)]. When the system has a crossed Z^3 nodal line, which is formed by two Z^3 nodal lines respectively with $n_z = 1$ and $n_x = 1$ [see Fig. 1(b)], one can expect that it may exhibit a Q1D feature, where the y -component longitudinal conductivity dominates the transport. Furthermore, the Z^3 nodal line is defined in momentum space while the layered and chain structures are defined in real space. Then, a natural question is: Does the ideal Z^3 nodal line or crossed Z^3 nodal line exist in AFM materials? If yes, what are its novel transport phenomena that distinguish it from conventional nodal line semimetals and metals with layered or chain structures?

In this work, we show that the AFM materials, including the existing compounds β -Fe₂(PO₄)O and

* These authors contributed equally to this work.

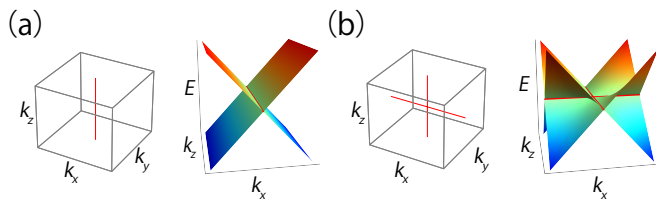


FIG. 1. (a) A Z^3 nodal line with $n_z = 1$. (b) A crossed Z^3 nodal line with $n_z = 1$, and $n_x = 1$.

$\text{Co}_2(\text{PO}_4)\text{O}$, and LiTi_2O_4 , are ideal topological Z^3 nodal net metals. Notice that these are not typical layered or Q1D chain materials. In these materials, each spin channel has a crossed Z^3 nodal line, formed by a Z^3 nodal line in $k_z = 0$ plane and two Z^3 nodal lines with $n_z = 1$. The two spin-polarized crossed nodal lines contact with each other at the BZ boundary, thereby resulting in a novel AFM Z^3 nodal net configuration, as shown in Fig. 3(c). The electronic structures of $\beta\text{-Fe}_2(\text{PO}_4)\text{O}$ and LiTi_2O_4 have been previously reported [46, 47]. The $\beta\text{-Fe}_2(\text{PO}_4)\text{O}$ has also been identified as an X-type antiferromagnetic material [48], characterized by sublattice-selective spin-polarized transport and spin torque. However, the influence of the AFM Z^3 nodal net on the spin transport of the systems has not been studied yet.

Via first-principles calculations, we find that for these materials, the Fermi level is located around the AFM Z^3 nodal net, and their spin longitudinal conductivity shows Q1D feature, i.e. the conductivity σ_{xx} (σ_{yy}) is approximately two orders of magnitude larger than σ_{yy} (σ_{xx}) and σ_{zz} in up-spin (down-spin) channel, leading to novel Q1D direction-dependent spin transport, which can not be found in both conventional 3D bulk materials and Q1D chain materials. Particularly, away from the AFM Z^3 nodal net, the spin conductivity still is anisotropic but increasingly lose the Q1D feature, indicating that this novel spin transport is closely related to the AFM Z^3 nodal net. We then use concrete examples to demonstrate our idea.

Example 1: $\beta\text{-Fe}_2(\text{PO}_4)\text{O}$ and $\text{Co}_2(\text{PO}_4)\text{O}$.—Material $\beta\text{-Fe}_2(\text{PO}_4)\text{O}$ is a mixed-valence iron oxyphosphate with valence states of $\text{Fe}^{2+}/\text{Fe}^{3+}$ [49–51]. Its single crystal has already been synthesized in the 1980s, and has experimentally confirmed as an AFM phase with the Néel temperature as high as 408 K [51].

The $\beta\text{-Fe}_2(\text{PO}_4)\text{O}$ has a tetragonal Bravais lattice, as shown in Fig. 2(a-b), from which one observes that the $\beta\text{-Fe}_2(\text{PO}_4)\text{O}$ is not a typical layered or chain material. The Fe and P atoms of $\beta\text{-Fe}_2(\text{PO}_4)\text{O}$ occupy the $8d$ and $4a$ Wyckoff sites, respectively. The O atoms take two Wyckoff sites: $4b$ and $16h$. The magnetic moments are mainly on the Fe sites with a magnitude of $\sim 4 \mu_B$ and the Néel vector is along the z axis [see Fig. 1(a)], consistent with our previous calculations [46]. The magnetic

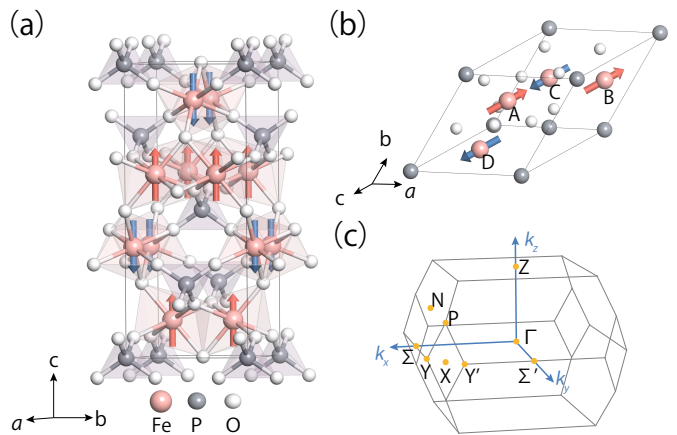


FIG. 2. (a) The conventional cell and (b) primitive cell of the $\beta\text{-Fe}_2(\text{PO}_4)\text{O}$ compound with AFM ordering. Red and blue arrows represent up-spin and down-spin magnetic moments, respectively. (c) The bulk Brillouin zone (BZ) with the high symmetry points labeled.

space group (MSG) for the $\beta\text{-Fe}_2(\text{PO}_4)\text{O}$ is No. 141.554 ($I4_1'/am'd$). Both the lattice constants and atomic positions are fully relaxed in our work. The optimized lattice constants are $a = b = 5.419 \text{ \AA}$ and $c = 12.657 \text{ \AA}$, which all agree with the experimental values ($a = b = 5.357 \text{ \AA}$ and $c = 12.505 \text{ \AA}$) [51].

Since the spin-orbit coupling (SOC) in $\beta\text{-Fe}_2(\text{PO}_4)\text{O}$ is negligible [52], we consider the spin-resolved band structure of the material without SOC, which is shown in Fig. 3(a). In the $k_z = 0$ plane, the $\beta\text{-Fe}_2(\text{PO}_4)\text{O}$ features a Z^3 Weyl nodal line in each spin channel, which is protected by the glide mirror symmetries $G_z = \{M_z | \frac{1}{2}0\frac{1}{2}\}$. The profiles of the two Weyl nodal lines are plotted in Fig. 3(b), from which one observes that the Weyl nodal line in the up-spin (down-spin) channel is very straight and traverses the BZ in k_y (k_x) direction. The two spin-resolved Weyl nodal lines contact with each other at the X point in the BZ. Moreover, for both spin channels, the two bands around the Fermi level are degenerate along two inequivalent P - X paths, leading to another two Z^3 nodal lines with $n_z = 1$, which are not only straight but also flat. These Z^3 nodal lines eventually form a Z^3 AFM nodal net, as shown in Fig. 3(c).

Since all the Z^3 Weyl nodal line in $\beta\text{-Fe}_2(\text{PO}_4)\text{O}$ are ideal and then exhibit extremely strong anisotropic feature, one can expect that the longitudinal conductivity σ_{xx}^\uparrow (σ_{yy}^\downarrow) of the up-spin (down-spin) channel in this material should be much larger than σ_{yy}^\uparrow (σ_{xx}^\downarrow) and σ_{zz}^\uparrow (σ_{zz}^\downarrow). In the absence of SOC, spin serves as a good quantum number, allowing for the conductivity of up-spin and down-spin electrons to be accurately defined and calculated. Thus, to directly explore the novel Q1D direction-dependent spin transport properties of the AFM Z^3 nodal net in $\beta\text{-Fe}_2(\text{PO}_4)\text{O}$, we calculate the spin-resolved

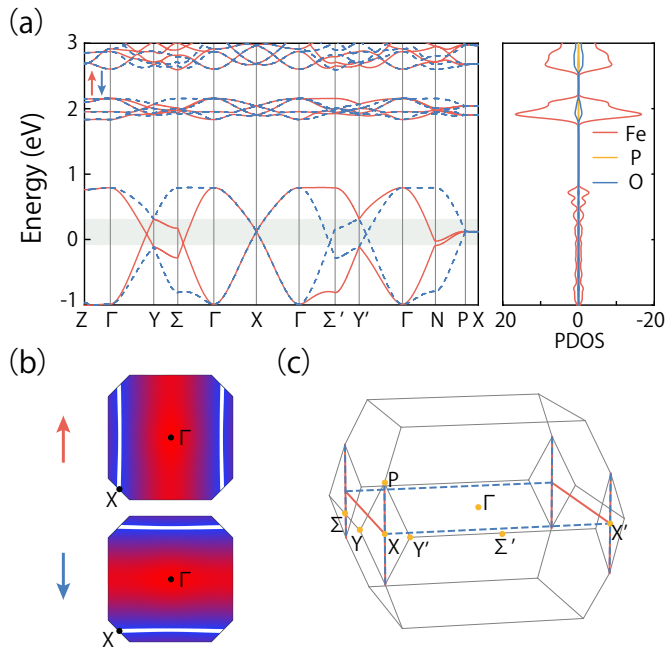


FIG. 3. (a) Electronic band structure and the projected density of states (PDOS) of $\beta\text{-Fe}_2(\text{PO}_4)\text{O}$. The energy region where the Z^3 AFM nodal net appears is highlighted by green. (b) The shapes of Z^3 nodal line in each spin channel. (c) The shape of Z^3 nodal net in the BZ. Red and blue lines represent up-spin and down-spin Weyl nodal lines.

longitudinal conductivities for different direction, and the obtained results are shown in Fig. 4. Three key features are observed.

First, the conductivities for each spin are not independent but are connected by $C_{4z}\mathcal{T}$ symmetry. Hence, we have $\sigma_{xx}^\uparrow = \sigma_{yy}^\downarrow$, $\sigma_{yy}^\uparrow = \sigma_{xx}^\downarrow$ and $\sigma_{zz}^\uparrow = \sigma_{zz}^\downarrow$.

Second, around the AFM nodal net, the conductivity of the system shows a novel spin-dependent signature that the longitudinal conductivity σ_{xx}^\uparrow (σ_{yy}^\downarrow) is dozens of times larger than the other two longitudinal conductivities. This means that while the electric current is isotropic, the spin current is strongly anisotropic and exhibits a Q1D signature in each spin channel. This phenomenon is completely different from the system with a chain structure, where both electric and spin currents should have a Q1D signature. Since the dominated transport directions for up-spin and down-spin are orthogonal, we can use the $\beta\text{-Fe}_2(\text{PO}_4)\text{O}$ to generate a current with strong spin polarization, and easily switch the spin polarization by rotating the sample 90 degrees along the z axis.

Third, away from the Z^3 AFM nodal net, the spin conductivity is still anisotropic but increasingly loses the Q1D signature. For the high-energy electrons, the σ_{xx} (σ_{yy}) of the up-spin (down-spin) and the other two conductivities are of the same order of magnitude (see Fig. 4). This strongly suggests that the spin-polarized Q1D

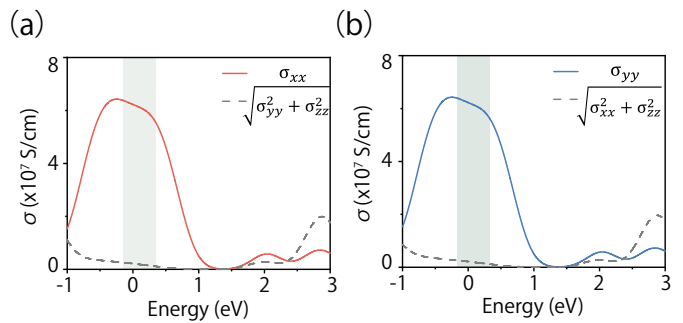


FIG. 4. The calculated conductivity of the $\beta\text{-Fe}_2(\text{PO}_4)\text{O}$ compound in (a) up-spin channel and (b) down-spin channel. The Z^3 AFM nodal net appears in the green shaded region.

transport is closely related to the Z^3 nodal net rather than the structure of the systems.

The $\text{Co}_2(\text{PO}_4)\text{O}$ has also been synthesized [53], and exhibits a similar crystalline structure, magnetic configuration, and electronic band with the $\beta\text{-Fe}_2(\text{PO}_4)\text{O}$ [52]. Particularly, the signature of Q1D spin transport is also significant in $\text{Co}_2(\text{PO}_4)\text{O}$. The detailed calculations can be found in Ref. [52].

Example 2: LiTi_2O_4 .—In addition to the $\beta\text{-Fe}_2(\text{PO}_4)\text{O}$ compound, the LiTi_2O_4 compound also has an AFM Z^3 nodal net near the Fermi level. As shown in Fig. 5(a), the lattice structure of LiTi_2O_4 belongs to a cubic Bravais lattice, which is different from that of $\beta\text{-Fe}_2(\text{PO}_4)\text{O}$. LiTi_2O_4 exhibits a AFM ground state with $141.554(I4'_1/am'd)$ magnetic symmetry [47]. The SOC effect in LiTi_2O_4 also is negligible.

Figure 5(c) plots the spin-resolved band structure of the LiTi_2O_4 without SOC. Scanning through the BZ gives the profile of the AFM Z^3 nodal net [see Fig. 5(b)], which includes one nodal line in the $k_z = 0$ plane and the two nodal lines along two inequivalent P - X paths for each spin channel. The obtained spin longitudinal conductivities are shown in Fig. 5(d-e), which have similar features to those in $\beta\text{-Fe}_2(\text{PO}_4)\text{O}$ and $\text{Co}_2(\text{PO}_4)\text{O}$. This again confirms that the Q1D spin transport is a common feature for the materials with an ideal Z^3 nodal net.

Lattice model of AFM Z^3 nodal net.—To further understand the Q1D spin transport, we establish a simple effective lattice model for the AFM Z^3 nodal net, based on $\beta\text{-Fe}_2(\text{PO}_4)\text{O}$. We consider a 3D tetragonal body-centred lattice with an AFM ordering, and assume that this lattice has the same MSG (No. 141.554) as the $\beta\text{-Fe}_2(\text{PO}_4)\text{O}$. The unit cell of the antiferromagnet includes an even number of lattice sites: up spins on half of sites and down spins on the remaining half. The lattice has four atoms with s -like orbitals per unit cell at $8d$ Wyckoff sites (labeled as $\{A, B, C, D\}$), which correspond to the positions occupied by the Fe atoms of $\beta\text{-Fe}_2(\text{PO}_4)\text{O}$ [see Fig. 2(b)].

The lattice has space group (SG) symmetry D_{4h}^{19} (e.g.

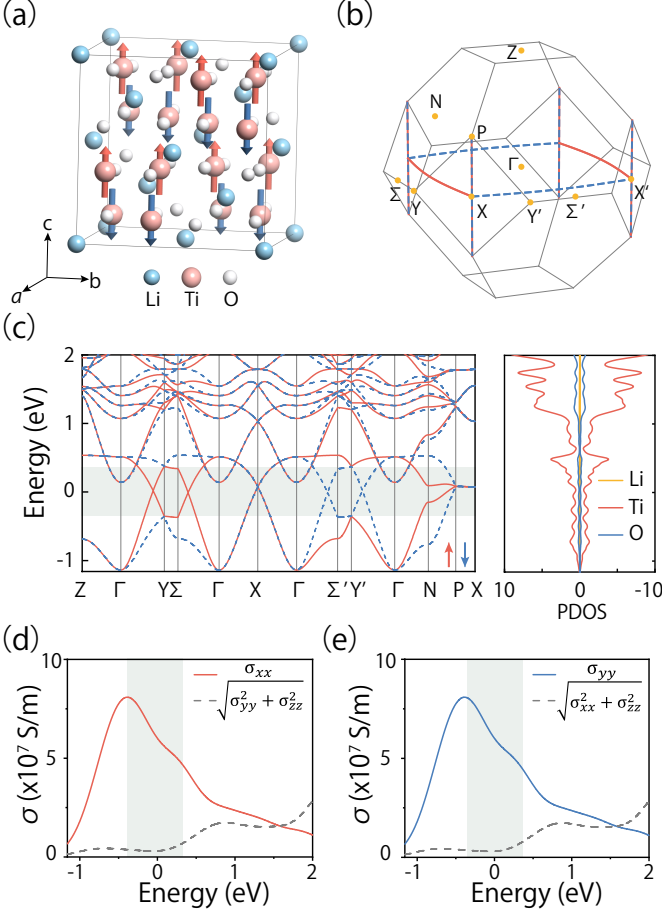


FIG. 5. (a) Crystal structures of the LiTi_2O_4 compound. Red and blue arrows represent up-spin and down-spin magnetic moments, respectively. (b) BZ and the shape of the Z^3 nodal net. Red and blue lines represent up-spin and down-spin Weyl nodal lines. (c) Electronic band structure and the PDOS of LiTi_2O_4 compound. The calculated conductivity in (d) up-spin channel and (e) down-spin channel. The Z^3 AFM nodal net appears in the green shaded region.

the SG 141), which is generated by a four-fold screw-rotation $S_{4z} = \{C_{4z} | \frac{1}{4} \frac{-1}{4} \frac{1}{4}\}$, a two-fold rotation C_{2x} and a spatial inversion P . Combining S_{4z}^2 and P leads to a glide mirror plane $G_z = \{M_z | \frac{1}{2} \frac{0}{2}\}$. Without anti-ferromagnetic ordering, the lattice also has time-reversal symmetry \mathcal{T} . In the absence of SOC, using the four sites as a basis, the symmetry operators can be represented as

$$S_{4z} = \begin{bmatrix} 0 & 0 & 1 & 0 \\ 0 & 0 & 0 & 1 \\ 0 & 1 & 0 & 0 \\ 1 & 0 & 0 & 0 \end{bmatrix}, C_{2x} = \begin{bmatrix} 1 & 0 & 0 & 0 \\ 0 & 1 & 0 & 0 \\ 0 & 0 & 0 & 1 \\ 0 & 0 & 1 & 0 \end{bmatrix}, \quad (1)$$

$P = \Gamma_{0,0}$ and $\mathcal{T} = \Gamma_{0,0}\mathcal{K}$ with $\Gamma_{i,j} = \sigma_i \otimes \sigma_j$. Here, σ_0 is identity matrix and σ denote the Pauli matrixes. The corresponding model Hamiltonian under these symmetry

constraints may be written as [54, 55]

$$\mathcal{H}_0 = \begin{bmatrix} H_1 & H' \\ H'^{\dagger} & H_2 \end{bmatrix}, \quad (2)$$

where $H_1 = t_1 \cos \frac{k_x+k_z}{2} \sigma_1$, $H_2 = t_1 \cos \frac{k_y+k_z}{2} \sigma_1$ and

$$H' = t_2 \begin{bmatrix} \cos \frac{k_z}{2} & \cos \frac{k_y}{2} \\ \cos \frac{k_x}{2} & \cos \frac{k_x+k_y+k_z}{2} \end{bmatrix}, \quad (3)$$

with t_i ($i = 1, 2$) the real parameters.

Then, we introduce spin degree of freedom and turn on a AFM ordering along z -direction [see Fig. 2(a)]. The AFM ordering breaks \mathcal{T} , S_{4z} and C_{2x} , while holds G_z , S_{2z} , P and the combined operation $S_{4z}\mathcal{T}$ and $C_{2x}\mathcal{T}$. To the leading order, the AFM Hamiltonian may be written as

$$\mathcal{H} = \mathcal{H}_0 s_0 + J_z s_z \Gamma_{3,0}, \quad (4)$$

with \mathbf{s} the Pauli matrixes acting on spin space and J_z denoting the strength of the AFM potential. When the AFM potential ($J_z > 0$) is much stronger than other hopping and energy terms, the eight bands are divided into two groups with each group including four bands. Since the two groups are separated in energy space by $2J_z$, the model (4) can be simplified as two effectively four-band model [56]. The basis of the upper subsystem is $(|A \uparrow\rangle, |B \uparrow\rangle, |C \downarrow\rangle, |D \downarrow\rangle)^T$ and that for the lower subsystem is $(|A \downarrow\rangle, |B \downarrow\rangle, |C \uparrow\rangle, |D \uparrow\rangle)^T$. We focus on the upper subsystem and omit J_z from it, as it only shifts the bands. Following the classical method [57], the upper four-band model can be expressed as

$$\mathcal{H}_{\text{eff}} = \frac{t_2^2}{4J_z} + \begin{bmatrix} H_1 & 0 \\ 0 & H_2 \end{bmatrix} + \frac{t_2^2}{4J_z} \begin{bmatrix} H'_1 & 0 \\ 0 & H'_2 \end{bmatrix}, \quad (5)$$

with

$$H'_1(\mathbf{k}) = 2(\cos \frac{k_x}{2} \cos \frac{k_z}{2} + \cos \frac{k_y}{2} \cos \frac{k_x+k_y+k_z}{2})\sigma_1 + \begin{bmatrix} \cos k_y + \cos k_z & 0 \\ 0 & \cos k_x + \cos(k_x+k_y+k_z) \end{bmatrix},$$

and $H'_2(k_x, k_y, k_z) = H'_1(k_y, k_x, k_z)$.

The band structure of \mathcal{H}_{eff} is calculated and plotted in Ref. [52], which qualitatively reproduces the band structure of $\beta\text{-Fe}_2(\text{PO}_4)\text{O}$. Our simple four-band effective model hence can serve as a good starting point for the further study of the physics of AFM Z^3 nodal net.

Conclusions.—We have predicted that the ideal AFM Z^3 nodal net can be achieved in realistic materials, and demonstrate that this topological structure can lead to novel Q1D spin transport, namely, the electrons with up-spin mainly flow along one direction while those with down-spin primarily flow in another direction normal to the previous direction. This remarkable feature contrast

with either conventional 3D bulk materials or Q1D chain materials, and can be easily detected by measuring the anisotropic spin resistance. Our work not only provides a good platform for exploring the novel physics of the AFM systems, but also shows great promise for applications in topological spintronics.

-
- [1] Y. Tokura, K. Yasuda, and A. Tsukazaki, Magnetic topological insulators, *Nat. Rev. Phys.* **1**, 126 (2019).
- [2] Y. Xu, L. Elcoro, Z.-D. Song, B. J. Wieder, M. G. Vergniory, N. Regnault, Y. Chen, C. Felser, and B. A. Bernevig, High-throughput calculations of magnetic topological materials, *Nature* **586**, 702 (2020).
- [3] L. Elcoro, B. J. Wieder, Z. Song, Y. Xu, B. Bradlyn, and B. A. Bernevig, Magnetic topological quantum chemistry, *Nat. Commun.* **12**, 5965 (2021).
- [4] B. A. Bernevig, C. Felser, and H. Beidenkopf, Progress and prospects in magnetic topological materials, *Nature* **603**, 41 (2022).
- [5] H. Sun, B. Xia, Z. Chen, Y. Zhang, P. Liu, Q. Yao, H. Tang, Y. Zhao, H. Xu, and Q. Liu, Rational design principles of the quantum anomalous hall effect in superlattice-like magnetic topological insulators, *Phys. Rev. Lett.* **123**, 096401 (2019).
- [6] Y. Deng, Y. Yu, M. Z. Shi, Z. Guo, Z. Xu, J. Wang, X. H. Chen, and Y. Zhang, Quantum anomalous Hall effect in intrinsic magnetic topological insulator MnBi_2Te_4 , *Science* **367**, 895 (2020).
- [7] H. Li, C.-Z. Chen, H. Jiang, and X. C. Xie, Coexistence of Quantum Hall and Quantum Anomalous Hall Phases in Disordered MnBi_2Te_4 , *Phys. Rev. Lett.* **127**, 236402 (2021).
- [8] H. Chen, Q. Niu, and A. H. MacDonald, Anomalous hall effect arising from noncollinear antiferromagnetism, *Phys. Rev. Lett.* **112**, 017205 (2014).
- [9] Y. Zhang, Y. Sun, H. Yang, J. Železný, S. P. P. Parkin, C. Felser, and B. Yan, Strong anisotropic anomalous Hall effect and spin Hall effect in the chiral antiferromagnetic compounds Mn_3X ($X = \text{Ge}, \text{Sn}, \text{Ga}, \text{Ir}, \text{Rh}, \text{and Pt}$), *Phys. Rev. B* **95**, 075128 (2017).
- [10] P. Li, J. Koo, W. Ning, J. Li, L. Miao, L. Min, Y. Zhu, Y. Wang, N. Alem, C.-X. Liu, Z. Mao, and B. Yan, Giant room temperature anomalous Hall effect and tunable topology in a ferromagnetic topological semimetal Co_2MnAl , *Nat. Commun.* **11**, 3476 (2020).
- [11] X. Zhou, R.-W. Zhang, X. Yang, X.-P. Li, W. Feng, Y. Mokrousov, and Y. Yao, Disorder- and topology-enhanced fully spin-polarized currents in nodal chain spin-gapless semimetals, *Phys. Rev. Lett.* **129**, 097201 (2022).
- [12] S. N. Guin, P. Vir, Y. Zhang, N. Kumar, S. J. Watzman, C. Fu, E. Liu, K. Manna, W. Schnelle, J. Gooth, *et al.*, Zero-Field Nernst Effect in a Ferromagnetic Kagome-Lattice Weyl-Semimetal $\text{Co}_3\text{Sn}_2\text{S}_2$, *Adv. Mater.* **31**, 1806622 (2019).
- [13] S. N. Guin, K. Manna, J. Nokoy, S. J. Watzman, C. Fu, N. Kumar, W. Schnelle, C. Shekhar, Y. Sun, J. Gooth, *et al.*, Anomalous Nernst effect beyond the magnetization scaling relation in the ferromagnetic Heusler compound Co_2MnGa , *NPG Asia Mater.* **11**, 16 (2019).
- [14] H. Zhang, C. Q. Xu, and X. Ke, Topological nernst effect, anomalous nernst effect, and anomalous thermal hall effect in the dirac semimetal Fe_3Sn_2 , *Phys. Rev. B* **103**, L201101 (2021).
- [15] Y. Pan, C. Le, B. He, S. J. Watzman, M. Yao, J. Gooth, J. P. Heremans, Y. Sun, and C. Felser, Giant anomalous Nernst signal in the antiferromagnet YbMnBi_2 , *Nat. Mater.* **21**, 203 (2022).
- [16] T. Suzuki, L. Savary, J.-P. Liu, J. W. Lynn, L. Balents, and J. G. Checkelsky, Singular angular magnetoresistance in a magnetic nodal semimetal, *Science* **365**, 377 (2019).
- [17] Y. Zhu, C.-Y. Huang, Y. Wang, D. Graf, H. Lin, S. H. Lee, J. Singleton, L. Min, J. C. Palmstrom, A. Bansil, B. Singh, and Z. Mao, Large anomalous Hall effect and negative magnetoresistance in half-topological semimetals, *Commun. Phys.* **6**, 346 (2023).
- [18] Z.-M. Yu, Z. Zhang, G.-B. Liu, W. Wu, X.-P. Li, R.-W. Zhang, S. A. Yang, and Y. Yao, Encyclopedia of emergent particles in three-dimensional crystals, *Sci. Bull.* **67**, 375 (2022).
- [19] Z. Zhang, G.-B. Liu, Z.-M. Yu, S. A. Yang, and Y. Yao, Encyclopedia of emergent particles in type-iv magnetic space groups, *Phys. Rev. B* **105**, 104426 (2022).
- [20] G.-B. Liu, Z. Zhang, Z.-M. Yu, S. A. Yang, and Y. Yao, Systematic investigation of emergent particles in type-iii magnetic space groups, *Phys. Rev. B* **105**, 085117 (2022).
- [21] Z. Zhang, Z.-M. Yu, and S. A. Yang, Magnetic higher-order nodal lines, *Phys. Rev. B* **103**, 115112 (2021).
- [22] H. Yan, Z. Feng, P. Qin, X. Zhou, H. Guo, X. Wang, H. Chen, X. Zhang, H. Wu, C. Jiang, and Z. Liu, Electric-Field-Controlled Antiferromagnetic Spintronic Devices, *Adv. Mater.* **32**, 1905603 (2020).
- [23] S. K. Kim, G. S. Beach, K.-J. Lee, T. Ono, T. Rasing, and H. Yang, Ferrimagnetic spintronics, *Nat. Mater.* **21**, 24 (2022).
- [24] H. Chen, L. Liu, X. Zhou, Z. Meng, X. Wang, Z. Duan, G. Zhao, H. Yan, P. Qin, and Z. Liu, Emerging Antiferromagnets for Spintronics, *Adv. Mater.* , 2310379 (2024).
- [25] N. Morali, R. Batabyal, P. K. Nag, E. Liu, Q. Xu, Y. Sun, B. Yan, C. Felser, N. Avraham, and H. Beidenkopf, Fermi-arc diversity on surface terminations of the magnetic Weyl semimetal $\text{Co}_3\text{Sn}_2\text{S}_2$, *Science* **365**, 1286 (2019).
- [26] G. Chang, S.-Y. Xu, X. Zhou, S.-M. Huang, B. Singh, B. Wang, I. Belopolski, J. Yin, S. Zhang, A. Bansil, H. Lin, and M. Z. Hasan, Topological Hopf and Chain Link Semimetal States and Their Application to Co_2MnGa , *Phys. Rev. Lett.* **119**, 156401 (2017).
- [27] R.-W. Zhang, X. Zhou, Z. Zhang, D.-S. Ma, Z.-M. Yu, W. Feng, and Y. Yao, Weyl monoloop semi-half-metal and tunable anomalous hall effect, *Nano Lett.* **21**, 8749 (2021).
- [28] Z. Feng, H. Yan, and Z. Liu, Electric-Field Control of Magnetic Order: From FeRh to Topological Antiferromagnetic Spintronics, *Adv. Electron. Mater.* **5**, 1800466 (2019).
- [29] H. Tsai, T. Higo, K. Kondou, T. Nomoto, A. Sakai, A. Kobayashi, T. Nakano, K. Yakushiji, R. Arita, S. Miwa, Y. Otani, and S. Nakatsuji, Electrical manipulation of a topological antiferromagnetic state, *Nature* **580**, 608–613 (2020).
- [30] T. Jungwirth, X. Marti, P. Wadley, and J. Wunderlich, Antiferromagnetic spintronics, *Nat. Nanotechnol.* **11**, 231

- (2016).
- [31] V. Baltz, A. Manchon, M. Tsoi, T. Moriyama, T. Ono, and Y. Tserkovnyak, Antiferromagnetic spintronics, *Rev. Mod. Phys.* **90**, 015005 (2018).
- [32] L. Šmejkal, Y. Mokrousov, B. Yan, and A. H. MacDonald, Topological antiferromagnetic spintronics, *Nat. Phys.* **14**, 242 (2018).
- [33] P. Tang, Q. Zhou, G. Xu, and S.-C. Zhang, Dirac fermions in an antiferromagnetic semimetal, *Nat. Phys.* **12**, 1100 (2016).
- [34] G. Hua, S. Nie, Z. Song, R. Yu, G. Xu, and K. Yao, Dirac semimetal in type-IV magnetic space groups, *Phys. Rev. B* **98**, 201116 (2018).
- [35] B. Wang, H. Gao, Q. Lu, W. Xie, Y. Ge, Y.-H. Zhao, K. Zhang, and Y. Liu, Type-I and type-II nodal lines coexistence in the antiferromagnetic monolayer CrAs₂, *Phys. Rev. B* **98**, 115164 (2018).
- [36] J. Liu and L. Balents, Anomalous Hall Effect and Topological Defects in Antiferromagnetic Weyl Semimetals: Mn₃Sn/Ge, *Phys. Rev. Lett.* **119**, 087202 (2017).
- [37] M. Yang, Y. Qian, D. Yan, Y. Li, Y. Song, Z. Wang, C. Yi, H. L. Feng, H. Weng, and Y. Shi, Magnetic and electronic properties of a topological nodal line semimetal candidate: HoSbTe, *Phys. Rev. Mater.* **4**, 094203 (2020).
- [38] D.-F. Shao, G. Gurung, S.-H. Zhang, and E. Y. Tsybal, Dirac nodal line metal for topological antiferromagnetic spintronics, *Phys. Rev. Lett.* **122**, 077203 (2019).
- [39] S. Malick, J. Singh, A. Laha, V. Kanchana, Z. Hossain, and D. Kaczorowski, Electronic structure and physical properties of EuAuAs single crystal, *Phys. Rev. B* **105**, 045103 (2022).
- [40] L. Huang, J. Zhu, W. Wu, J. Cao, Z. Zhang, Y. Jiao, Y. Liu, L. Wang, and S. A. Yang, Antiferromagnetic nodal loop and strain-controllable magnetic phase transition in monolayer MnAl, *Appl. Phys. Lett.* **121**, 213101 (2022).
- [41] J. Zhan, J. Li, W. Shi, X.-Q. Chen, and Y. Sun, Coexistence of weyl semimetal and weyl nodal loop semimetal phases in a collinear antiferromagnet, *Phys. Rev. B* **107**, 224402 (2023).
- [42] T. P. T. Nguyen and K. Yamauchi, Ab initio prediction of anomalous Hall effect in antiferromagnetic CaCrO₃, *Phys. Rev. B* **107**, 155126 (2023).
- [43] Z. Zhu, H. Liu, Y. Ge, Z. Zhang, W. Wu, C. Xiao, and S. A. Yang, Third-order charge transport in a magnetic topological semimetal, *Phys. Rev. B* **107**, 205120 (2023).
- [44] S. Li, Z.-M. Yu, Y. Liu, S. Guan, S.-S. Wang, X. Zhang, Y. Yao, and S. A. Yang, Type-II nodal loops: Theory and material realization, *Phys. Rev. B* **96**, 081106 (2017).
- [45] Z.-M. Yu, W. Wu, X.-L. Sheng, Y. X. Zhao, and S. A. Yang, Quadratic and cubic nodal lines stabilized by crystalline symmetry, *Phys. Rev. B* **99**, 121106 (2019).
- [46] T. He, X. Zhang, W. Meng, L. Jin, X. Dai, and G. Liu, Topological nodal lines and nodal points in the antiferromagnetic material β -Fe₂PO₅, *J. Mater. Chem. C* **7**, 12657 (2019).
- [47] T. He, X. Zhang, Y. Liu, X. Dai, L. Wang, and G. Liu, Potential antiferromagnetic Weyl nodal line state in LiTi₂O₄ material, *Phys. Rev. B* **104**, 045143 (2021).
- [48] S.-S. Zhang, Z.-A. Wang, B. Li, S.-H. Zhang, R.-C. Xiao, L.-X. Liu, X. Luo, W. Lu, M. Tian, Y. Sun, *et al.*, X-type antiferromagnets, *arXiv preprint arXiv:2310.13271* (2023).
- [49] A. Modaressi, A. Courtois, R. Gerardin, B. Malaman, and C. Gleitzer, Fe₂PO₅, un phosphate de fer de valence mixte. Préparation et études structurale, mössbauer et magnétique, *J. Solid State Chem.* **40**, 301 (1981).
- [50] B. Ech-Chahed, F. Jeannot, B. Malaman, and C. Gleitzer, Préparation et étude d'une variété basse température de l'oxyphosphate de fer de valence mixte β -Fe₂(PO₄)O et de NiCr(PO₄)O: Un cas d'échange électronique rapide, *J. Solid State Chem.* **74**, 47 (1988).
- [51] M. Ijjaali, B. Malaman, C. Gleitzer, J. Warner, J. Hriljac, and A. Cheetham, Stability, structure refinement, and magnetic properties of β -Fe₂(PO₄)O, *J. Solid State Chem.* **86**, 195 (1990).
- [52] See Supplemental Material for the calculation methods, the band structure of the β -Fe₂(PO₄)O compound with spin-orbit coupling, detailed analysis of the Co₂(PO₄)O compound, and the band structure of the lattice model.
- [53] G. Wang, M. Valldor, E. T. Spielberg, and A.-V. Mudring, Ionothermal Synthesis, Crystal Structure, and Magnetic Study of Co₂PO₄OH Isostructural with Caminite, *Inorg. Chem.* **53**, 3072 (2014).
- [54] Z. Zhang, Z.-M. Yu, G.-B. Liu, and Y. Yao, MagneticTB: A package for tight-binding model of magnetic and non-magnetic materials, *Comput. Phys. Commun.* **270**, 108153 (2022).
- [55] Z. Zhang, Z.-M. Yu, G.-B. Liu, Z. Li, S. A. Yang, and Y. Yao, MagneticKP: A package for quickly constructing $k \cdot p$ models of magnetic and non-magnetic crystals, *Comput. Phys. Commun.* **290**, 108784 (2023).
- [56] J. Wang, Antiferromagnetic dirac semimetals in two dimensions, *Phys. Rev. B* **95**, 115138 (2017).
- [57] R. Winkler, S. Papadakis, E. De Poortere, and M. Shayegan, *Spin-orbit coupling in two-dimensional electron and hole systems*, Vol. 41 (Springer, 2003).

Supplemental Material for “ Quasi-one-dimensional spin transport in antiferromagnetic Z^3 nodal net metals ”

Tingli He,^{1,2} Lei Li,² Chaoxi Cui,² Run-Wu Zhang,² Zhi-Ming Yu,² Guodong Liu,¹ and Xiaoming Zhang¹

¹*School of Materials Science and Engineering, Hebei University of Technology, Tianjin 300130, China*

²*Key Lab of advanced optoelectronic quantum architecture and measurement (MOE), Beijing Key Lab of Nanophotonics & Ultrafine Optoelectronic Systems, and School of Physics, Beijing Institute of Technology, Beijing 100081, China*

I. CALCULATION METHODS

The first-principles calculations in the work are based on the density functional theory (DFT) using the Vienna ab initio Simulation Package [1, 2]. The generalized gradient approximation (GGA) of the Perdew-BurkeErnzerhof (PBE) functional was modeled as the exchange-correlation potential [3]. The cutoff energy was set at 500 eV, and a Monkhorst-Pack k -point mesh of $15 \times 15 \times 15$ was used for the Brillouin zone (BZ) sampling [4]. The energy and force convergence criteria were set as 10^{-7} eV and 0.001 eV/Å in the calculation. The GGA + U method was employed to describe the strongly correlated Fe $3d$ orbitals [5, 6]. The effective U value of Fe and Ti atom were set to 4 eV, Co was set to 3 eV. The electrical conductivity was calculated using the Boltzmann equation in the Wannier90 code [7, 8], employing a $100 \times 100 \times 100$ crystal momentum mesh and a relaxation time τ of 500 fs ($\Gamma = 8.27$ meV).

II. BAND STRUCTURE WITH THE SPIN-ORBIT COUPLING INCLUDED OF β -Fe₂(PO₄)O

The band structure with spin-orbit coupling (SOC) included is shown in Fig. S1 for the β -Fe₂(PO₄)O compound. One can see that the two spin channels are coupled, but the band crossings are still maintained. Due to the weak SOC effect of the system, only a small band gap opens up on the X point. Therefore, we mainly discussed the results of β -Fe₂(PO₄)O compound without SOC in the main text.

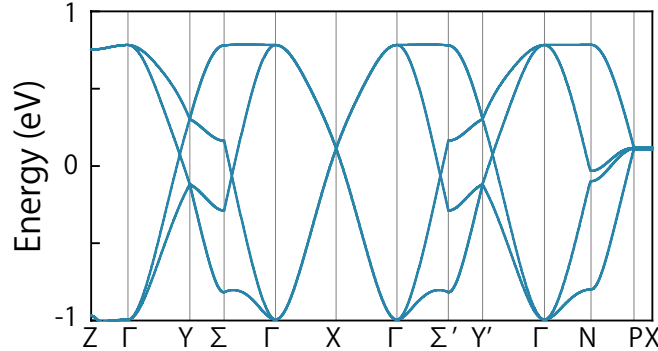


FIG. S1: The band structure with the SOC included of β -Fe₂(PO₄)O compound.

III. DETAILED ANALYSIS OF THE CO₂(PO₄)O COMPOUND

The Co₂(PO₄)O compound has a tetragonal Bravais lattice, as shown in Fig. S2(a). The Co₂(PO₄)O compound has a similar Z^3 nodal net near the Fermi level under the AFM ground state. The spin-resolved band structure and projected density of states (PDOS) without SOC are shown in Fig. S2(c). The corresponding k -paths are displayed in Fig. S2(b). In the $k_z = 0$ plane, Co₂(PO₄)O has a Z^3 Weyl nodal line in each spin channel, which is protected by mirror symmetries. The two spin-resolved Weyl nodal lines contact with each other at the X point in the BZ [see the Fig. S2(b)]. Moreover, around the Fermi level, the two bands of each spin channel are degenerate along the P - X path, leading to another two Z^3 nodal lines with $n_z = 1$, which are not only straight but also flat. These Z^3 nodal lines eventually form a Z^3 AFM nodal net, as shown in Fig. S2(b).

The conductivity of different spin channels are shown in Fig. S2(d-e). One can observe that the longitudinal conductivity σ_{xx}^\uparrow (σ_{yy}^\downarrow) is dozens of times larger than the other two longitudinal conductivities. Near the Fermi level, σ_{xx} dominates transport in the up-spin channel, while σ_{yy} dominates transport in the down-spin channel, leading to novel Q1D direction-dependent spin transport. However, moving away from the nodal line will result in the loss of these Q1D direction-dependent transport properties. This strongly indicates that the Q1D spin transport is caused by the AFM Z^3 nodal net. It can be believed that similar structures such as $M_2PO_4O(F)$ ($M = \text{Metal}$) can also exhibit similar Z^3 nodal nets. If the ideal Z^3 nodal net is near the Fermi level, the system will have novel low-dimensional transport properties.

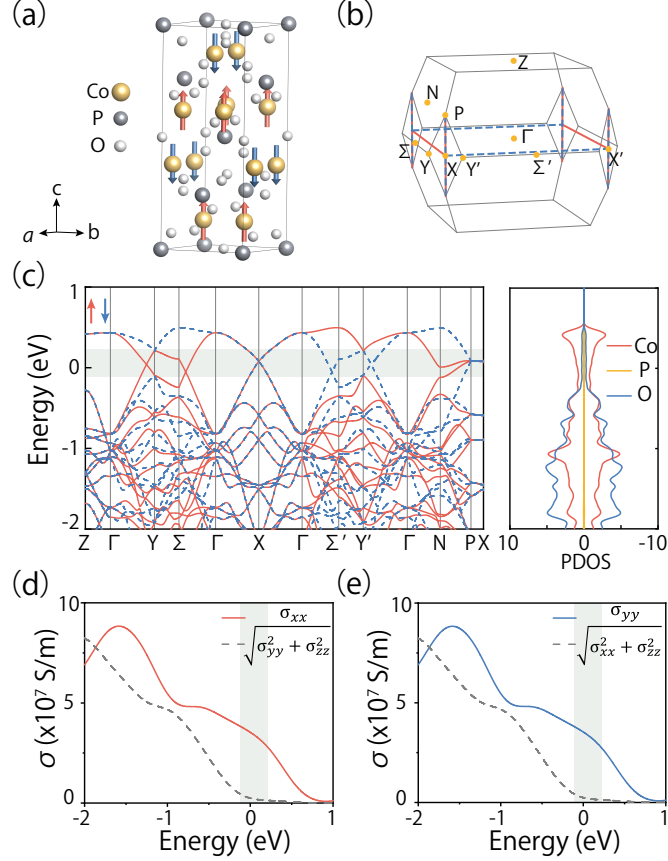


FIG. S2: (a) Crystal structures of $\text{Co}_2(\text{PO}_4)\text{O}$ compound. Red and blue arrows represent up-spin and down-spin magnetic moments, respectively. (b) The shape of Z^3 nodal net in the BZ. Red and blue lines represent up-spin and down-spin Weyl nodal lines. (c) Electronic band structure and the projected density of states PDOS of $\text{Co}_2(\text{PO}_4)\text{O}$ compound. The Calculated conductivity of $\text{Co}_2(\text{PO}_4)\text{O}$ in (d) up-spin channel and (e) down-spin channel. The Z^3 AFM nodal net appears in the green shaded region.

IV. THE BAND STRUCTURE OF LATTICE MODEL

The band structure of \mathcal{H}_{eff} in the main text is shown in the Fig. S3, which qualitatively reproduces the band structure of $\beta\text{-Fe}_2(\text{PO}_4)\text{O}$.

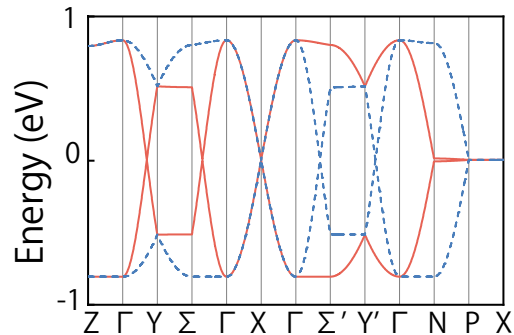


FIG. S3: Calculated electronic band structure of \mathcal{H}_{eff} in the main text with $t_1 = 0.8$, $t_2 = 0.2$, $J_z = 2$. The up-spin and down-spin bands are denoted by red and blue curves.

-
- [1] G. Kresse and J. Furthmüller, Efficient iterative schemes for ab initio total-energy calculations using a plane-wave basis set, *Phys. Rev. B* **54**, 11169 (1996).
 - [2] G. Kresse and J. Furthmüller, Efficiency of ab-initio total energy calculations for metals and semiconductors using a plane-wave basis set, *Comp. Mater. Sci.* **6**, 15 (1996).
 - [3] J. P. Perdew, K. Burke, and M. Ernzerhof, Generalized Gradient Approximation Made Simple, *Phys. Rev. Lett.* **77**, 3865 (1996).
 - [4] H. J. Monkhorst and J. D. Pack, Special points for brillouin-zone integrations, *Phys. Rev. B* **13**, 5188 (1976).
 - [5] V. I. Anisimov, J. Zaanen, and O. K. Andersen, Band theory and Mott insulators: Hubbard U instead of Stoner I, *Phys. Rev. B* **44**, 943 (1991).
 - [6] S. L. Dudarev, G. A. Botton, S. Y. Savrasov, C. J. Humphreys, and A. P. Sutton, Electron-energy-loss spectra and the structural stability of nickel oxide: An LSDA+U study, *Phys. Rev. B* **57**, 1505 (1998).
 - [7] A. A. Mostofi, J. R. Yates, Y.-S. Lee, I. Souza, D. Vanderbilt, and N. Marzari, Wannier90: A tool for obtaining maximally-localised Wannier functions, *Computer Physics Communications* **178**, 685 (2008).
 - [8] A. A. Mostofi, J. R. Yates, G. Pizzi, Y.-S. Lee, I. Souza, D. Vanderbilt, and N. Marzari, An updated version of wannier90: A tool for obtaining maximally-localised Wannier functions, *Computer Physics Communications* **185**, 2309 (2014).